ACS APPLIED MATERIALS & INTERFACES

Research Article

Cite This: ACS Appl. Mater. Interfaces 2019, 11, 37842−37849

www.acsami.org

Enhanced Electrochemical Performance of the Lithium-Manganese-Rich Cathode for Li-Ion Batteries with Na and F CoDoping

Panawan Vanaphuti,[†] Jiajun Chen,[†] Jiayu Cao,[†] Karly Bigham,[†] Bin Chen,[†] Lufeng Yang,[‡] Hailong Chen,[‡] and Yan Wang*[,†]

[†]Department of Mechanical Engineering, Worcester Polytechnic Institute, Worcester, Massachusetts 01609, United States

[‡]Woodruff School of Mechanical Engineering, Georgia Institute of Technology, Atlanta, Georgia 30332, United States

Supporting Information

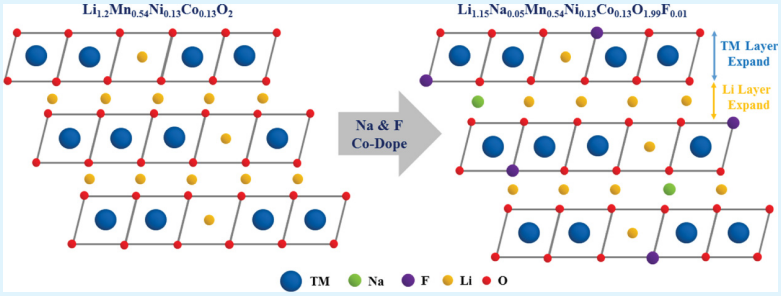

ABSTRACT: The lithium-manganese-rich layered oxide cathode (LMR-NMC), $xLi_2MnO_3\cdot(1-x)LiMO_2$ (M = Co, Ni, and Mn), is on demand because of its high specific capacity of over 250 mA h g^{-1} between the voltage range 2.0−4.8 V (vs Li/Li^+). Because of the requirement of activating the Li_2MnO_3 phase in the first cycle, oxygen extraction from the lattice structure occurs. Consequently, capacity fading and voltage fading during cycling are still major obstacles to the commercialization of LMR-NMC in battery applications. Here, codoping Na and F into LMR-NMC via facile hydroxide coprecipitation followed by solid-state reaction is introduced. Na and F are partially substituted into Li and O sites, respectively. These dopant ions enlarge the Li slab, which in turn eases Li diffusion and minimizes oxygen loss, thereby stabilizing the structure. The codoped sample exhibits both high capacity retention (97%) and high voltage retention (91%) over 100 cycles with an initial discharge capacity of 260 mA h g^{-1} at 0.1 C. Compared to other reports on LMR-NMC as obtained by coprecipitation, results from this study show the best capacity retention. The developed codoping approach may provide a new strategy for designing high-performance LMR-NMC cathodes for next-generation lithium ion batteries.

KEYWORDS: *co-precipitation, co-dope, cathode, lithium ion battery, sodium, fluorine*

1. INTRODUCTION

Because of the large demand of electric vehicles and grid energy storage systems, many ongoing research studies are focusing on the improvement of energy density, capacity, cycling stability, and rate performances of Li-ion batteries. The lithium-manganese-rich layered oxide cathode (LMR-NMC), $xLi_2MnO_3\cdot(1-x)LiMO_2$ (M = Co, Ni, and Mn), is one of the promising cathode materials for the near future owing to a capacity of over 250 mA h g^{-1} and an energy density of over 1000 W h kg^{-1} when cycling in the voltage range 2.0−4.8 V (vs Li/Li^+). LMR-NMC can be described as two phases, a trigonal $LiMO_2$ ($R\bar{3}m$ space group) and Li_2MnO_3 ($C2/m$ space group).[1] It has been reported that particle morphology and crystallinity have a major impact on the performance of the cathode material.[2−5] Among various methods used to synthesize LMR-NMC, the facile coprecipitation technique had been chosen in this work as it is simple, well-controlled, and easy to scale-up.[6] Carbonate coprecipitation was used by many groups because of its fast and ease of morphology control; however, the obtained particles were more fragile and had lower electrode density compared to the hydroxide route. Hydroxide process does not have these issues, although the reaction is more complex and it is difficult to control the structure.[7]

Two main challenges still remain before these materials can be fully applied commercially: capacity fading and voltage fading.[8−12] Many factors contribute to these phenomena, but the most pronounced ones are oxygen release as Li_2O during Li_2MnO_3 activation to active MnO_2 component and phase transformation from layered to spinel structure from side reaction when charged to 4.8 V.[12] Regardless of chemical activation and surface coating methods, doping suitable ions are of interest to overcome these issues.[13] Many studies on doping have been investigated, which include both cation and anion aspects. Some examples of doping cations are Na, K, Ca, Fe, V, Cr, Cd, Al, Si, Ru, Rb, Zr, and La and doping anions are B, F, and S.[14,15] Although most of these ions provide

Received: August 11, 2019
Accepted: September 27, 2019
Published: September 27, 2019

DOI: 10.1021/acsami.9b13838
ACS Appl. Mater. Interfaces 2019, 11, 37842−37849

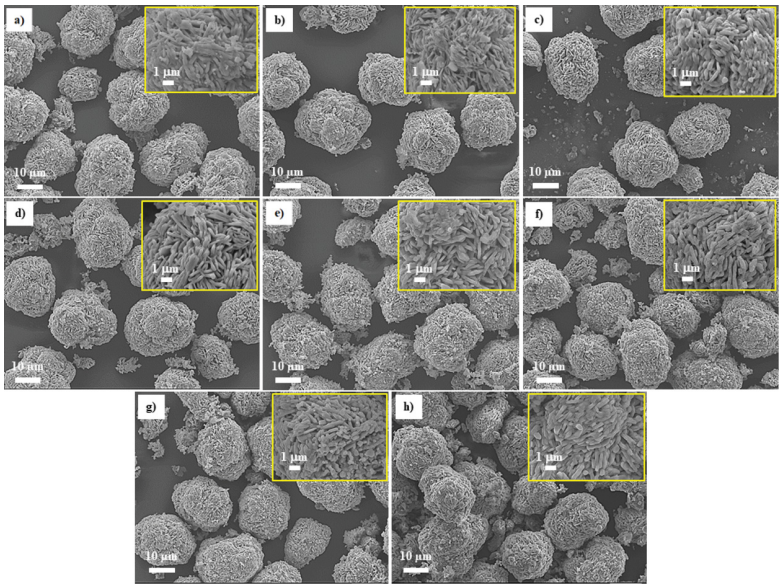

Figure 1. Particle morphology from SEM of (a) PR, (b) N30, (c) N50, (d) N70, (e) F05, (f) F10, (g) F15, and (h) CD.

impressive performance, cost and abundance are also important aspects. Out of all the doping ions, Na and F are commonly studied as cation and anion substitutions, respectively, as they are inexpensive, abundant, and have a proper ionic radius. Na ions partially replace the lithium site, while F ions partially replace the oxygen site (as M−F rather than M−O bonds) to enhance rate capability and cycling stability of LMR-NMC. Moreover, recent studies combine cation and anion cosubstitution in order to maximize properties of each ion.[16−22] Examples of recent studies on LMR-NMC with ion doping from various techniques and pristine-synthesized via coprecipitation are compared with this work (see Table S1).

Here, we focus on the structure, properties, and electrochemical performances of Na- and F-codoped LMR-NMC, $Na_xLi_{1.2-x}Mn_{0.54}Ni_{0.13}Co_{0.13}O_{2-y}F_y$, synthesized via hydroxide coprecipitation followed by solid-state reaction. Initially, LMR-NMC with a single dopant ratio was examined, and best performance of each dopant was then selected in order to maximize the capability of the cathode material. Our codoped sample showed impressive capacity retention, and to our knowledge, our work shows the best capacity retention compared to other studies with the coprecipitation method. For example, our codoped sample shows capacity retention (97%) and voltage retention (91%) over 100 cycles with initial discharge capacity of 260 mA h g^{-1} at 0.1 C. Based on this discovery, synthesis via hydroxide coprecipitation and codoping method shows that the best capacity retention in improving the performance of LMR-NMC was identified, allowing us to enhance the possibility of using LMR-NMC commercially in next-generation batteries.

2. EXPERIMENTAL SECTION

2.1. Sample Preparation. The $Mn_{0.54}Ni_{0.13}Co_{0.13}(OH)_2$ precursor was synthesized via a hydroxide coprecipitation method. Stoichiometric amounts of 2.0 M $MnSO_4{\cdot}4H_2O$, $NiSO_4{\cdot}6H_2O$, and $CoSO_4{\cdot}7H_2O$ (GFS Chemicals) were dissolved in 0.5 M NH_4OH (32%, EMD Millipore) in a 1 L continuous stirred tank reactor. NaOH (VWR) and NH_4OH (1:1 ratio) were added to the reactor with a controlled rate. NaOH solution was used to adjust the pH, while NH_4OH maintained the pH stability and acted as chelating agents. The coprecipitation reaction was synthesized at 50 °C with the controlled pH between 10 and 11. The hydroxide precipitate was filtered, washed with distilled water to remove salt residuals, and air-dried at 120 °C overnight. Then, the precursor was hand-grinded using a mortar with stoichiometric ratios of Li_2CO_3 (GFS Chemicals), LiF (98+%, Alfa Aesar), and Na_2CO_3 (VWR) and underwent a two-step sintering process: 450 °C for 5 h and 800−900 °C for 14−20 h. Both heating and cooling rates were maintained at 2 °C min^{-1}. In order to compensate for the loss of lithium ions during annealing at high temperature, 5% excess of Li_2CO_3 were added. A total of eight samples were obtained, including $Li_{1.2}Mn_{0.54}Ni_{0.13}Co_{0.13}O_2$ (PR), $Na_xLi_{1.2-x}Mn_{0.54}Ni_{0.13}Co_{0.13}O_2$ (x = 0.03, 0.05, and 0.07, named as N30, N50, and N70, respectively), $Li_{1.2}Mn_{0.54}Ni_{0.13}Co_{0.13}F_yO_{2-y}$ (y = 0.005, 0.01, and 0.015, named as F05, F10, and F15, respectively), and $Na_{0.05}Li_{1.15}Mn_{0.54}Ni_{0.13}Co_{0.13}F_{0.01}O_{1.99}$ (CD).

2.2. Material Characterization. The morphology and crystal structure of the prepared samples were examined by X-ray diffraction (XRD; PANalytical Empyrean, Cu Kα, λ = 1.54 Å radiation, 45 kV, and 40 mA), scanning electron microscopy (SEM; JEOL JSM 7000F), and in situ XRD (Bruker D8 ADVANCE diffractometer, Mo Kα, λ = 0.709 Å radiation). The lattice parameters and quantity of each phase were calculated by Rietveld refinement using FullProf Suite program under the assumption that structure compositions were $LiMO_2$ ($R\bar{3}m$ space group) and Li_2MnO_3 ($C2/m$ space group). The element compositions were analyzed by inductively coupled plasma optical emission spectroscopy (ICP−OES; PerkinElmer Optima 8000), energy dispersive spectroscopy coupled with SEM (EDS−SEM), and X-ray photoelectron spectroscopy (XPS; PHI VersaProbe II).

2.3. Electrochemical Measurement. All cathode electrodes were prepared with 80 wt % cathode powder, 10 wt % Super C65 Carbon Black (Imerys Graphite & Carbon), and 10 wt % polyvinylidene fluoride (MTI) dissolved in *N*-methyl-2-pyrrolidone (NMP) (Sigma-Aldrich). After mixing homogenously, the slurry was casted on an aluminum foil using a 100 mm film casting doctor blade (MTI) and dried at 60 °C overnight. Diameter electrodes (14 mm) were punched and calendared to get a final thickness of 50 μm with an active material loading of 3.5−4.0 mg cm^{-2}. The samples were dried at 80 °C overnight in a vacuum oven to remove access NMP. All 2032 coin cells were assembled in an argon-filled glovebox (H_2O, O_2 < 0.1 ppm) with the lithium metal as the anode. $LiPF_6$ (1 M) in ethylene carbonate /ethylmethyl carbonate (3:7 weight ratio) and 25 μm trilayer polypropylene−polyethylene−polypropylene membrane (MTI) were used as the electrolyte and separator, respectively.

DOI: 10.1021/acsami.9b13838
ACS Appl. Mater. Interfaces 2019, 11, 37842−37849

Electrochemical performance was tested using the land battery testing system (LAND CT2001A). All cells were charged and discharged at room temperature between the potential range of 2.0 and 4.8 V versus Li/Li^+. Electrochemical impedance spectroscopy (EIS) data and cyclic voltammetry (CV) data were obtained from an electrochemical analyzer (Bio-Logic SAS VMP3) using the EC-Lab V10.40 program. The frequency range and amplitude were 10 mHz to 100 kHz and 10 mV, respectively.

3. RESULTS

3.1. Morphology, Elemental Composition, and Crystal Structure Analysis. Figure 1a–h shows the SEM images of eight samples. All samples contain plate-like primary particles, with thicknesses of ~250 nm, which agglomerate into spherical secondary particles ranging from 15 to 17 μm. With the F dopant, the primary plate is denser compared to the pristine and Na dopant, which is consistent with the report of other cathode materials with F.[23−28] Doping with F also shows more agglomeration of primary and secondary particles resulting in a higher tap density and a lower surface area. This may be attributed to the fluoride source (LiF) that has an impact on the crystallization rate.[24,29] Moreover, all doped samples still maintain spherical secondary structures and uniform distribution. In order to determine the distribution of each element, Figure S1 illustrates the EDS–SEM mapping of pristine and doped Na samples. The cross section of the images provides the evidence of these elements present throughout the particles. F is not showed in EDS mapping because of the overlapping of Mn Lα energy with F Kα, and the Mn wt % is much higher than F wt % in the samples. The presence of both Na and F is examined by XPS surface analysis, as shown in Figure 2 with expansion in Figure 2b,c.

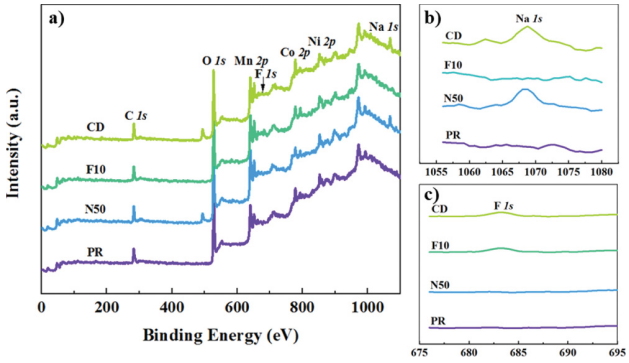

Figure 2. XPS analysis showing (a) survey scan, (b) Na 1s expansion, and (c) F 1s expansion.

Table 1 denotes elemental wt %. While the data represent only the surface, the trend can be observed. With the F dopant, the O wt % decreases, which is consistent with XRD refinement data, in which F partially replaces the O site. The same aspect applies for the Na dopant, in which Li wt % decreases. The exact ratio of elements is identified by ICP–OES (see Table S2).

The XRD pattern of each sample is illustrated in Figure 3. The main diffraction peaks corresponded to the layered structure indexed as hexagonal α-$NaFeO_3$ (space group $R\bar{3}m$, $LiMO_2$). The minor diffraction peaks at the Bragg angle between 20° and 23° represent the monoclinic structure (space group $C2/m$) from the Li_2MnO_3 compound. This is due to the $LiMn_6$ unit with short-range cation ordering within the transition-metal layer.[24] All the dopant samples show no impurity phase or a structural change, and peak positions are very similar to that of the pristine sample. Also, (003) and (110) planes show a noticeable shift to lower angles for both Na and F doped samples as a result of the expansion of c-axis and a/b-axis, respectively. Table 2 and Figure S2 represent the results calculated by the Rietveld refinement using both $R\bar{3}m$ (high symmetry) and $C2/m$ space groups (low symmetry). Both a-axis and c-axis rise as the F content increases, which is consistent with previous studies.[16,24] As Na content increases, lattice parameters increase because the Na ionic radius is bigger than that of the Li ion.[30,31] In the case of F, to maintain the charge balance when O^{2-} is substituted with F^-, partial reduction of transition metal ions needs to occur by reducing $Mn^{4+}/Ni^{3+}/Co^{3+}$ to $Mn^{3+}/Ni^{2+}/Co^{2+}$ (see Table S3).[24] These reduced transition-metal ions have a larger radius than the one with a higher oxidation state, conforming to the increase in lattice parameters. Similarly, the ratio of $I(003)/(104)$, related to the degree of Li/Ni mixing, also increases for doped samples. The higher $I(003)/(104)$ value indicates a lower cation mixing between Ni^{2+} and Li^+ and more ordering of the layered structure.[32] The oxygen occupancy, $z(O)$, is lower in F-doped samples confirming replacement of F^- on the O^{2-} site. Doped samples show a higher percent of the monoclinic structure resulting in higher discharge capacity because of more activation of the Li_2MnO_3 component during the first charge at a high voltage. Hence, better performance of doped samples is achieved compared to the pristine one because of the improvement of Li diffusivity, which is expected to lead to better electrochemical properties.

3.2. Electrochemical Studies. In order to observe the improvement of the prepared samples, rate and cycle performances were measured at a voltage range between 2.5 and 4.8 V versus the Li metal as the anode at room temperature for all samples. Relatively, a low percent (0.5–1.5%) of the F dopant has been used in this study as F easily reacts with Li to form LiF on the surface instead of F doped into the bulk. Therefore, a lower percent of LiF (F source) is

Table 1. Elemental Weight Percent from XPS Surface Analysis

sample	C 1s	Li 1s	O 1s	Mn 2p	Co $2p_1$	Ni $2p_3$	F 1s
PR	15.90	5.56	38.90	21.16	6.83	11.65	0.00
N50	14.45	4.74	37.79	31.82	5.27	8.93	0.12
F10	14.35	5.80	36.99	28.53	4.50	9.84	2.57
CD	14.82	4.42	35.94	25.98	7.65	11.18	2.44
RSF	0.314	0.028	0.733	2.688	1.056	2.309	1.00
corrected RSF	6.906	0.599	16.502	66.597	26.506	58.385	116.266
mean	14.88	5.13	36.66	26.87	6.06	10.40	1.28
SD	0.71	0.66	1.74	4.50	1.44	1.24	0.99

DOI: 10.1021/acsami.9b13838
ACS Appl. Mater. Interfaces 2019, 11, 37842–37849

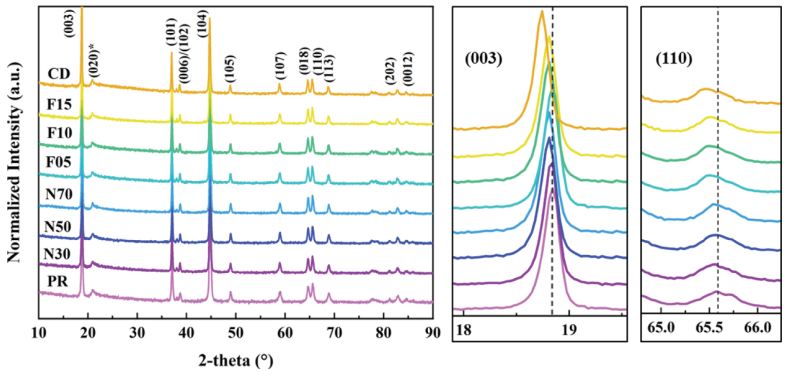

Figure 3. XRD patterns of prepared samples where the annotation symbol (*) represents the characteristic peak of the monoclinic structure (space group $C2/m$) with expansion of (003) and (110) planes.

Table 2. Data from Refinement Calculations

sample	symmetry	wt %	unit volume (Å^3)	a (Å)	c (Å)	c/a	$I(003)/(104)$	z(O)	R_{wp} (%)	Chi2
PR	$R\bar{3}m$	93.53	100.084	2.8500(1)	14.2280(0)	4.9923	1.68	0.2474(8)	4.90	2.44
	$C2/m$	6.47	201.466							
N50	$R\bar{3}m$	93.29	100.138	2.8504(5)	14.2311(1)	4.9925	1.73	0.2477(0)	5.14	2.47
	$C2/m$	6.71	201.611							
F10	$R\bar{3}m$	92.99	100.202	2.8510(2)	14.2309(0)	4.9915	1.78	0.2446(7)	5.06	2.50
	$C2/m$	7.01	201.683							
CD	$R\bar{3}m$	92.66	100.234	2.8512(7)	14.2366(4)	4.9931	1.80	0.2457(9)	4.78	2.08
	$C2/m$	7.34	202.065							

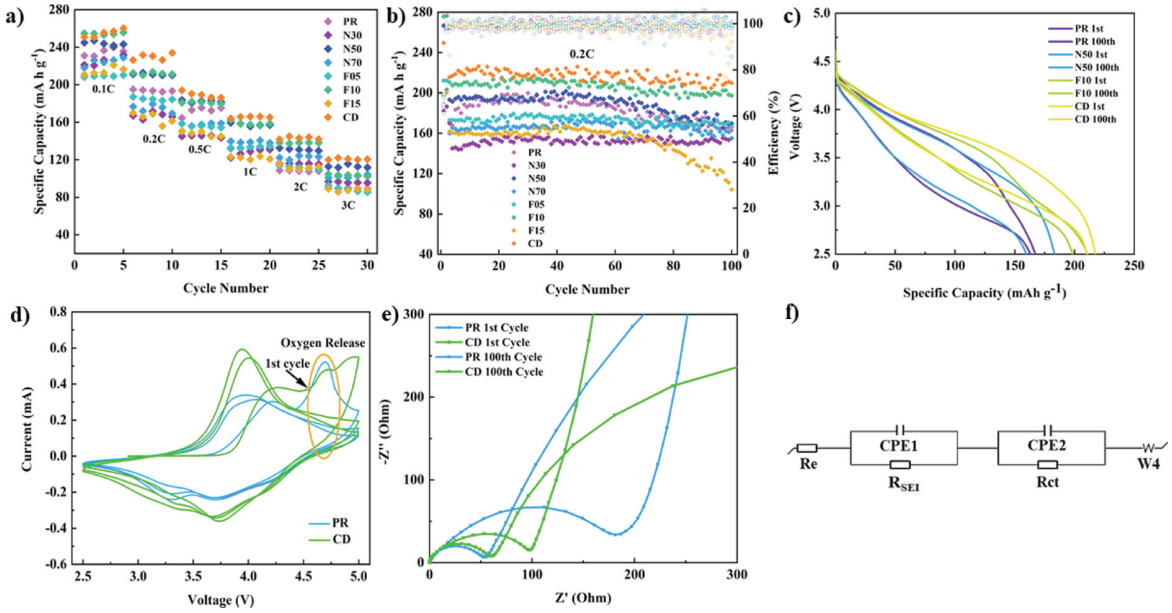

Figure 4. Electrochemical performance of undoped and doped samples (a) rate performance, (b) 100th cycle, (c) plot between specific capacity vs. voltage of the 1st and 100th cycle, (d) CV curve for PR and CD with a scan rate of 0.1 mV s^{-1}, (e) EIS curve of PR and CD, and (f) equivalent circuit model.

used in order to avoid this surface formation.[29,33] Figure 4a,b shows that the suitable percent for Na is 5% and F is 1%, which provides discharge capacity after 100 cycles of 169.6 and 197.3 mA h g^{-1} at 0.2 C. Among all, CD shows the best rate performance and capacity retention compared to other samples. After the 100th cycle, the discharge capacity is 209.8 mA h g^{-1} with capacity retention of 97% compared to the single dopant N50 and F10, which gives 87 and 94%, respectively. Accurate numbers are provided in Tables S4 and S5, while Figures S3 and S4 present the initial voltage profile and the midvoltage plot for PR and CD. Referring to Figure 4c, the discharge curves between the 1st and 100th cycle for PR, N50, F10, and CD samples correspond to the voltage fading characteristics of the cathode material. While all samples have voltage decay at a certain level, F and CD display notable voltage retention after 100 cycles of 91%. This is probably due to the partial replacement of F^- on the oxygen site and reduction of oxygen extraction during Li_2MnO_3 activation.

DOI: 10.1021/acsami.9b13838
ACS Appl. Mater. Interfaces 2019, 11, 37842−37849

This result is consistent with the CV curve (Figure 4d). Around 4.6 V, CD has a lower amount of oxygen oxidation peak in contrast with PR during the first cycle. These peaks disappear in the second cycle because of the irreversibility of oxygen loss from this material. Additionally, CD has a higher oxidation peak of Ni^{2+}/Co^{3+} to Ni^{4+}/Co^{4+} around 3.9 V, resulting in higher specific capacity. Reduction of Ni^{4+}/Co^{4+} to Ni^{2+}/Co^{3+} happens at 3.7 V. Significant reduction of Mn^{4+} is shown for the PR sample at 3.3 V for charge compensation from oxygen loss.[27,34] For CD, this peak is not noticeable.

EIS measurements (Figure 4e) provide a clearer clarification between PR and CD for the 1st cycle and after the 100th cycle. Using the equivalent circuit model (Figure 4f), Table 3 shows

Table 3. Data from the EIS Fitting Curve

sample	cycle	R_e (Ω)	R_{ct} (Ω)	W_4 (Ω $s^{-1/2}$)
PR	1st	56.76	136.2	99.46
	100th	25.51	968.2	85.39
CD	1st	66.22	79.31	88.39
	100th	15.38	52.18	61.59

the calculation from fitting of the EIS curve, using the EC-Lab V10.40 program. CD validates its capability over PR with lower electrolyte Ohmic resistance (R_e), charge-transfer resistance (R_{ct}), and the Warburg impedance (W_4). W_4 defines the kinetic mechanism of Li^+ ions in the bulk materials; a smaller number means a faster diffusion rate. R_e of the initial cycle is high for both samples. This may be due to the freshly assembled cells with the uncycled Li electrode. After the 100th cycle, CD has less R_e = 15.38 Ω, R_{ct} = 52.18 Ω, and W_4 = 61.59 Ω $s^{-1/2}$ than PR, which gives R_e = 25.51 Ω, R_{ct} = 968.2 Ω, and W_4 = 85.39 Ω $s^{-1/2}$.

A clear comparison among PR, N50, F10, and CD samples is represented as a bar chart (Figure 5a). As predicted, samples with F dopant give the highest percent voltage retention equaling 91% for F10 and CD samples. For capacity fading, PR and CD retain 97% after 100 cycles. The difference is that CD shows higher specific capacity than PR. According to these factors, CD provides the best energy density retention. In comparison to other works with the doping technique, our work also displays impressive results in maintaining the capacity over 100 cycles, and it is the best regarding to the coprecipitation technique. The plot is shown in Figure 5b (from Table S1). In addition, the high stability in the structure of our LMR-NMC may result from the hydroxide coprecipitation synthesis route, which offer a plate-like structure of the primary particle and improve electrode density. This has also been elucidated in previous studies, in which they compare between carbonate coprecipitation and hydroxide coprecipitation processes.[5,35,36]

3.3. Studies of the Effect of CoDoping after Cycle.

Further analysis between PR and CD samples are carried out via *in situ* XRD during the 1st cycle and 101th cycle by applying voltage between 2.5 and 4.8 V to elucidate the structural evolution upon lithiation/delithiation upon extended electrochemical cycling. Figures 6 and S5 illustrate (003), (104), and (105) planes with the corresponding voltage profiles on the right. Full profiles are shown in Figure S6. Because of the thick electrodes used in testing *in situ* XRD (~90 μm) to provide a higher signal, the initial columbic efficiency is lower than expected. This may create larger resistance and a higher degree of polarization.[37,38] Although the (110) plane is directly correlated to the *ab* plane, the signal is relatively weak for shifting observation, so the (104) plane has been used in the discussion. Upon lithium deintercalation, while the (003) peak continuously shifts to lower Bragg angles from 3.57 to ~4.5 V, the (104) peak progressively shifts to higher angles from 3.57 to 4.8 V, suggesting that the *c*-axis expands and the *ab* plane contracts (in relation to *c*-axis) because of increasing electrostatic repulsion between the oxygen slabs and the smaller ionic radius of Ni^{4+} (0.62 Å), respectively.[20,31] However, the (003) peak slightly shifts back to higher angles when the voltage was further increased to 4.8 V. This finding can be associated with the slight slipping of the transition-metal (MO_2) layers to alleviate the increasing electrostatic repulsion between them. During discharge, a very similar evolution of the peaks is found but with the opposite trend, indicating a good reversible structural evolution upon lithium deintercalation/intercalation. It is noteworthy that the CD sample displays more alteration in the *c*-axis than PR. This may relate to the larger strain along the *ab* plane because of the inclusion of doped ions.

Interestingly, the (105) peak slightly shifts to higher angles during the charge and begins to split into two peaks when voltage increases to ~4.1 V, revealing a two-phase reaction occurring in the electrode materials upon cycling. However, the observed two peaks merge into one at the following discharge and shift reversely to the lower angle side,

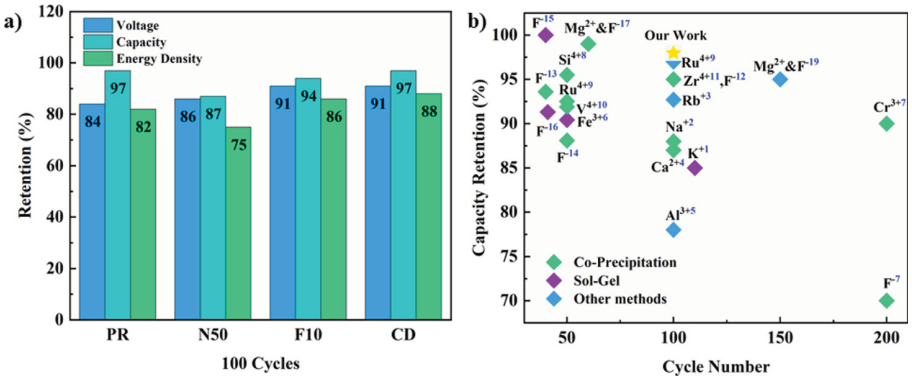

Figure 5. (a) Bar chart showing comparison of capacity fading, voltage fading, and energy density for PR, N50, F10, and CD and (b) comparison between capacity retention and the cycle number of LMR-NMC with other works.

DOI: 10.1021/acsami.9b13838
ACS Appl. Mater. Interfaces 2019, 11, 37842−37849

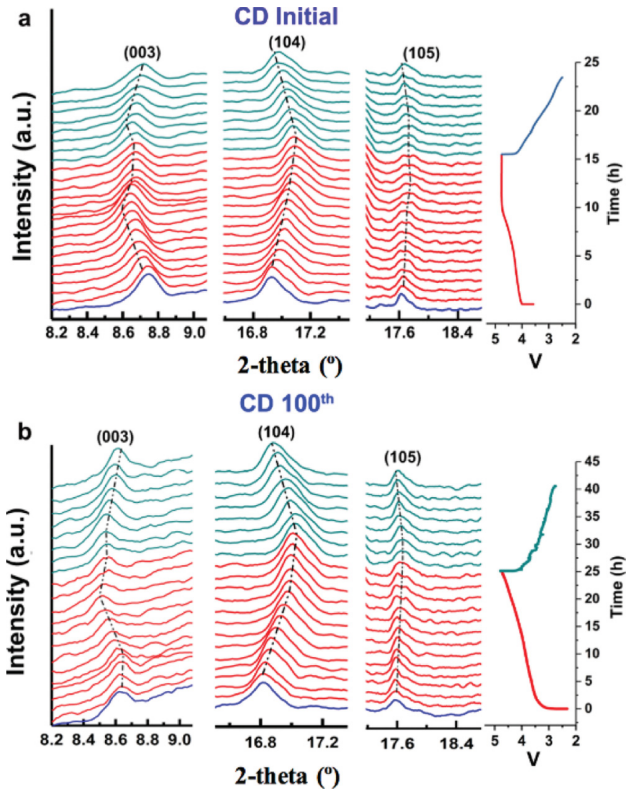

Figure 6. *In situ* XRD spectra of the CD sample collected with the molybdenum target (0.709 Å) during charge and discharge at C/20 between 4.80−2.50 V and 4.80−2.74 V for (a) initial electrode (b) cycled electrode after 100 cycles, respectively. The XRD pattern collected at the open circuit potential state of the in situ battery is plotted in blue.

demonstrating the good reversibility of the lithium deintercalation/intercalation-induced structural change.

In comparison to PR, the CD sample shows better crystallinity in the *in situ* XRD spectra, evident by the sharper line width, which also implies a better structural stability and lesser mechanical damages induced by cycling. Moreover, CD spectra of both (003) and (104) planes do not shift. Thus, such high repeatability of *in situ* XRD spectra of CD after long-term cycling reveals its high structural stability. This may relate to the inclusion of dope ions into the structure, which facilitates the intercalation process because of expansion of the Li slab, which is consistent with XRD refinement and electrochemical performance data.

After 100 cycles, the coin cells were disassembled to obtain the electrodes for the additional structure study. These electrodes were washed with dimethyl carbonate solvent to remove electrolyte contamination and dried at 100 °C overnight prior to SEM analysis. SEM images of the PR and CD electrodes after the cycle are illustrated in Figure 7. In contrast to CD, the PR electrode surface shows the fracture of cathode particles leading to higher capacity/voltage fade after 100 cycles for PR than the CD sample.

4. CONCLUSIONS

In summary, PR and doped samples were successfully synthesized via the hydroxide coprecipitation route followed by a two-step sintering process to obtain cathode powders. The SEM image and the XRD pattern prove that the Na and F dopant do not significantly impact the structure of the LMR-NMC. Although the primary particles become denser with F compared to PR and Na doping, XRD refinement shows minor deviations in lattice parameters. Initially, LMR-NMC with a single dopant of Na and F ratio was examined, and the best performance of each dopant amount was then selected in order to optimize the capability of the cathode material. XPS analysis verifies the presence of Na and F in the samples. Regarding the electrochemical studies, CD has the best performance in terms of capacity (97%) and voltage retention (91%) after 100 cycles at 0.2 C with an initial discharge capacity of 260 mA h g^{-1} at 0.1 C. This is the result from the inclusion of Na and F into the structure that enhanced structural stability and widening of the Li slab to facilitate the Li diffusion proven by refinement data.

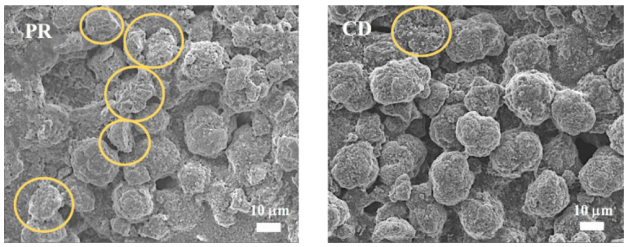

Figure 7. SEM images of PR and CD electrodes after 100 cycles. The yellow circle represents the fracture of particles.

Furthermore, the samples are also analyzed by *in situ* XRD and SEM after 100 cycles. The data shows consistent results with electrochemical performance demonstrating that CD can minimize the phase transformation from oxygen extraction during the activation cycle and while cycling. According to these results, syntheses via the hydroxide coprecipitation and codoping method show the best capacity retention in improving the performance of LMR-NMC, allowing us to enhance the possibility of using LMR-NMC commercially in next-generation batteries.

■ ASSOCIATED CONTENT

Supporting Information

The Supporting Information is available free of charge on the ACS Publications website at DOI: 10.1021/acsami.9b13838.

SEM−EDS, Rietveld refinement data, initial charge and discharge curve, midvoltage profile, full spectra of in situ XRD for PR and CD, comparison table with other studies, ICP−OES elemental analysis, and half-cell test data for all samples (PDF)

■ AUTHOR INFORMATION

Corresponding Author

*E-mail: yanwang@wpi.edu.

ORCID

Hailong Chen: 0000-0001-8283-2860

Yan Wang: 0000-0003-1060-2956

Author Contributions

The manuscript was written through contributions of all authors. All authors have given approval to the final version of the manuscript.

Notes

The authors declare no competing financial interest.

DOI: 10.1021/acsami.9b13838
ACS Appl. Mater. Interfaces 2019, 11, 37842−37849

■ ACKNOWLEDGMENTS

The authors would like to thank Dr. Feng Wang from the Brookhaven National Laboratory for providing thoughtful discussions and gratefully acknowledge the Department of Chemistry, Chulalongkorn University in collaboration with Bangkok Bank Public Co., Ltd. (Thailand) for a graduate fellowship awarded to P.V.

■ REFERENCES

(1) Thackeray, M. M.; Kang, S.-H.; Johnson, C. S.; Vaughey, J. T.; Benedek, R.; Hackney, S. A. Li2MnO3-Stabilized LiMO2 (M = Mn, Ni, Co) Electrodes for Lithium-Ion Batteries. *J. Mater. Chem.* **2007**, *17*, 3112−3125.

(2) Li, J.; Li, J.; Yu, T.; Ding, F.; Xu, G.; Li, Z.; Zhao, Y.; Kang, F. Stabilizing the Structure and Suppressing the Voltage Decay of Li[Li0.2Mn0.54Co0.13Ni0.13]O2 Cathode Materials for Li-ion Batteries via Multifunctional Pr Oxide Surface Modification. *Ceram. Int.* **2016**, *42*, 18620−18630.

(3) Shukla, A. K.; Ramasse, Q. M.; Ophus, C.; Kepaptsoglou, D. M.; Hage, F. S.; Gammer, C.; Bowling, C.; Gallegos, P. A. H.; Venkatachalam, S. Effect of Composition on the Structure of Lithium- and Manganese-Rich Transition Metal Oxides. *Energy Environ.* **2018**, *11*, 830−840.

(4) Zuo, Y.; Ma, J.; Jiang, N.; Xia, D. Effects of Particle Size on Voltage Fade for Li-Rich Mn-Based Layered Oxides. *ACS Omega* **2018**, *3*, 11136−11143.

(5) Huang, L.; Liu, L.; Wu, H.; Wang, Y.; Liu, H.; Zhang, Y. Optimization of Synthesis Parameters for Uniform Sphere-like Li1.2Mn0.54Ni0.13Co0.13O2 as High Performance Cathode Material for Lithium Ion Batteries. *J. Alloys Compd.* **2019**, *775*, 921−930.

(6) Zheng, J. M.; Wu, X. B.; Yang, Y. A comparison of preparation method on the electrochemical performance of cathode material Li[Li0.2Mn0.54Ni0.13Co0.13]O2 for lithium ion battery. *Electrochim. Acta* **2011**, *56*, 3071−3078.

(7) Wang, D.; Belharouak, I.; Koenig, G. M.; Zhou, G.; Amine, K. Growth Mechanism of Ni0.3Mn0.7CO3 Precursor for High Capacity Li-ion Battery Cathodes. *J. Mater. Chem.* **2011**, *21*, 9290−9295.

(8) Chen, C.-J.; Pang, W. K.; Mori, T.; Peterson, V. K.; Sharma, N.; Lee, P.-H.; Wu, S.-h.; Wang, C.-C.; Song, Y.-F.; Liu, R.-S. The Origin of Capacity Fade in the Li2MnO3·LiMO2 (M = Li, Ni, Co, Mn) Microsphere Positive Electrode: An Operando Neutron Diffraction and Transmission X-ray Microscopy Study. *J. Am. Chem. Soc.* **2016**, *138*, 8824−8833.

(9) Singer, A.; Zhang, M.; Hy, S.; Cela, D.; Fang, C.; Wynn, T. A.; Qiu, B.; Xia, Y.; Liu, Z.; Ulvestad, A.; Hua, N.; Wingert, J.; Liu, H.; Sprung, M.; Zozulya, A. V.; Maxey, E.; Harder, R.; Meng, Y. S.; Shpyrko, O. G. Nucleation of Dislocations and Their Dynamics in Layered Oxide Cathode Materials During Battery Charging. *Nat. Energy* **2018**, *3*, 641−647.

(10) Shpyrko, S.; Cho, W.; Jin, W.; Hwang, J.; Yoon, M.; Yoo, Y.; Nam, G.; Jang, H.; Han, J. G.; Choi, N. S.; Kim, M. G.; Cho, J. Understanding Voltage Decay in Lithium-Excess Layered Cathode Materials Through Oxygen-Centred Structural Arrangement. *Nat. Commun.* **2018**, *9*, 3285−3295.

(11) Hu, E.; Yu, X.; Lin, R.; Bi, X.; Lu, J.; Bak, S.; Nam, K.-W.; Xin, H. L.; Jaye, C.; Fischer, D. A.; Amine, K.; Yang, X.-Q. Evolution of Redox Couples in Li- and Mn-Rich Cathode Materials and Mitigation of Voltage Fade by Reducing Oxygen Release. *Nat. Energy* **2018**, *3*, 690−698.

(12) Teufl, T.; Strehle, B.; Müller, P.; Gasteiger, H. A.; Mendez, M. A. Oxygen Release and Surface Degradation of Li- and Mn-Rich Layered Oxides in Variation of the Li2MnO3Content. *J. Electrochem. Soc.* **2018**, *165*, A2718−A2731.

(13) Shin, Y.; Kan, W. H.; Aykol, M.; Papp, J. K.; McCloskey, B. D.; Chen, G.; Persson, K. A. Alleviating Oxygen Evolution from Li-Excess Oxide Materials Through Theory-Guided Surface Protection. *Nat. Commun.* **2018**, *9*, 4597−4605.

(14) Pan, H.; Zhang, S.; Chen, J.; Gao, M.; Liu, Y.; Zhu, T.; Jiang, Y. Li- and Mn-Rich Layered Oxide Cathode Materials for Lithium-Ion Batteries: A Review from Fundamentals to Research Progress and Applications. *Mol. Syst. Des. Eng.* **2018**, *3*, 748−803.

(15) Hu, S.; Pillai, A. S.; Liang, G.; Pang, W. K.; Wang, H.; Li, Q.; Guo, Z. Li-Rich Layered Oxides and Their Practical Challenges: Recent Progress and Perspectives. *Electrochem. Energy Rev.* **2019**, *2*, 277−311.

(16) Lim, S. N.; Seo, J. Y.; Jung, D. S.; Park, S.; Bin, S. H.; Yeon, S. H. The Crystal Structure and Electrochemical Performance of Li1.167Mn0.548Ni0.18Co0.105O2 Composite Cathodes Doped and Co-Doped with Mg and F. *J. Electroanal. Chem.* **2015**, *740*, 88−94.

(17) Kumar, S. K.; Ghosh, S.; Martha, S. K. Synergistic Effect of Magnesium and Fluorine Doping on the Electrochemical Performance of Lithium-Manganese Rich (LMR)-Based Ni-Mn-Co-Oxide (NMC) Cathodes for Lithium-Ion Batteries. *Ionics* **2017**, *23*, 1655−1662.

(18) Ming, L.; Zhang, B.; Cao, Y.; Zhang, J. F.; Wang, C. H.; Wang, X. W.; Li, H. Effect of Nb and F Co-Doping on Li1.2Mn0.54Ni0.13-Co0.13O2 Cathode Material for High-Performance Lithium-Ion Batteries. *Front. Chem.* **2018**, *6*, 1−12.

(19) Li, M.; Wang, H.; Zhao, L.; Zhou, Y.; Zhang, F.; He, D. Improving the Electrochemical Performance of Lithium-Rich Oxide Layer Material with Mg and La Co-Doping. *J. Alloys Compd.* **2019**, *782*, 451−460.

(20) Chen, G.; An, J.; Meng, Y.; Yuan, C.; Matthews, B.; Dou, F.; Shi, L.; Zhou, Y.; Song, P.; Wu, G.; Zhang, D. Cation and Anion Co-Doping Synergy to Improve Structural Stability of Li- and Mn-Rich Layered Cathode Materials for Lithium-Ion Batteries. *Nano Energy* **2019**, *57*, 157−165.

(21) Liu, D.; Fan, X.; Li, Z.; Liu, T.; Sun, M.; Qian, C.; Ling, M.; Liu, Y.; Liang, C. A cation/anion co-doped Li1.12Na0.08Ni0.2Mn0.6O1.95F0.05 cathode for lithium ion batteries. *Nano Energy* **2019**, *58*, 786−796.

(22) Liu, Y.; Fan, X.; Zhang, Z.; Wu, H.-H.; Liu, D.; Dou, A.; Su, M.; Zhang, Q.; Chu, D. Enhanced Electrochemical Performance of Li-Rich Layered Cathode Materials by Combined Cr Doping and LiAlO2 Coating. *ACS Sustainable Chem. Eng.* **2019**, *7*, 2225−2235.

(23) Zheng, J.; Wu, X.; Yang, Y. Improved Electrochemical Performance of Li[Li0.2Mn0.54Ni0.13Co0.13]O2 Cathode Material by Fluorine Incorporation. *Electrochim. Acta* **2013**, *105*, 200−208.

(24) Li, L.; Song, B. H.; Chang, Y. L.; Xia, H.; Yang, J. R.; Lee, K. S.; Lu, L. Retarded phase transition by fluorine doping in Li-rich layered Li 1.2 Mn 0.54 Ni 0.13 Co 0.13 O 2 cathode material. *J. Power Sources* **2015**, *283*, 162−170.

(25) Song, J. H.; Kapylou, A.; Choi, H. S.; Yu, B. Y.; Matulevich, E.; Kang, S. H. Suppression of Irreversible Capacity Loss in Li-Rich Layered Oxide by Fluorine Doping. *J. Power Sources* **2016**, *313*, 65−72.

(26) Kumar, S. K.; Ghosh, S.; Ghosal, P.; Martha, S. K. Synergistic Effect of 3D Electrode Architecture and Fluorine Doping of Li1.2Ni0.15Mn0.55Co0.1O2 for High Energy Density Lithium-Ion Batteries. *J. Power Sources* **2017**, *356*, 115−123.

(27) Wang, Y.; Gu, H.-T.; Song, J.-H.; Feng, Z.-H.; Zhou, X.-B.; Zhou, Y.-N.; Wang, K.; Xie, J.-Y. Suppressing Mn Reduction of Li-Rich Mn-Based Cathodes by F-Doping for Advanced Lithium-Ion Batteries. *J. Phys. Chem. C* **2018**, *122*, 27836−27842.

(28) Xiang, W.; Zhu, C.-Q.; Zhang, J.; Shi, H.; Liang, Y.-T.; Yu, M.-H.; Zhu, X.-M.; He, F.-R.; Lv, G.-P.; Guo, X.-D. Synergistic Coupling Effect of Sodium and Fluorine Co-Substitution on Enhancing Rate Capability and Cycling Performance of Ni-Rich Cathode for Lithium Ion Battery. *J. Alloys Compd.* **2019**, *786*, 56−64.

(29) Richards, W. D.; Dacek, S. T.; Kitchaev, D. A.; Ceder, G. Fluorination of Lithium-Excess Transition Metal Oxide Cathode Materials. *Adv. Energy Mater.* **2018**, *8*, 1701533.

(30) Dong, X.; Xu, Y.; Xiong, L.; Sun, X.; Zhang, Z. Sodium substitution for partial lithium to significantly enhance the cycling stability of Li 2 MnO 3 cathode material. *J. Power Sources* **2013**, *243*, 78−87.

DOI: 10.1021/acsami.9b13838
ACS Appl. Mater. Interfaces 2019, 11, 37842−37849

(31) Chen, S.; Chen, Z.; Xia, M.; Cao, C.; Luo, Y. Toward Alleviating Voltage Decay by Sodium Substitution in Lithium-Rich Manganese-Based Oxide Cathodes. *ACS Appl. Energy Mater.* **2018**, *1*, 4065−4074.
(32) Li, H.; Guo, H.; Wang, Z.; Wang, J.; Li, X.; Chen, N.; Gui, W. Improving Rate Capability and Decelerating Voltage Decay of Li-Rich Layered Oxide Cathodes by Chromium Doping. *Int. J. Hydrogen Energy* **2018**, *43*, 11109−11119.
(33) Lee, J. H.; Papp, J. K.; Clément, R. J.; Sallis, S.; Kwon, D.; Shi, T.; Yang, W.; McCloskey, B. D.; Ceder, G. Mitigating Oxygen Loss to Improve the Cycling Performance of High Capacity Cation-Disordered Cathode Materials. *Nat. Commun.* **2017**, *8*, 981−991.
(34) Lu, Z.; Beaulieu, L. Y.; Thomas, C. L.; Dahn, J. R. Synthesis, Structure, and Electrochemical Behavior of Li[Ni[sub x]Li[sub 1/3−2x/3]Mn[sub 2/3−x/3]]O[sub 2]. *J. Electrochem. Soc.* **2002**, *149*, A778−A822.
(35) Wang, D.; Belharouak, I.; Ortega, L. H.; Zhang, X.; Xu, R.; Zhou, D.; Zhou, G.; Amine, K. Synthesis of High Capacity Cathodes for Lithium-Ion Batteries by Morphology-Tailored Hydroxide Co-Precipitation. *J. Power Sources* **2015**, *274*, 451−457.
(36) Pimenta, V.; Sathiya, M.; Batuk, D.; Abakumov, A. M.; Giaume, D.; Cassaignon, S.; Larcher, D.; Tarascon, J.-M. Synthesis of Li-Rich NMC: A Comprehensive Study. *Chem. Mater.* **2017**, *29*, 9923−9936.
(37) Qian, Y.; Niehoff, P.; Börner, M.; Grützke, M.; Mönnighoff, X.; Behrends, p.; Nowak, S.; Winter, M.; Schappacher, F. M. Influence of electrolyte additives on the cathode electrolyte interphase (CEI) formation on LiNi 1/3 Mn 1/3 Co 1/3 O 2 in half cells with Li metal counter electrode. *J. Power Sources* **2016**, *329*, 31−40.
(38) Zhang, J.-N.; Li, Q.; Wang, Y.; Zheng, J.; Yu, X.; Li, H. Dynamic Evolution of Cathode Electrolyte Interphase (CEI) on High Voltage LiCoO2 Cathode and its Interaction with Li Anode. *Energy Storage Mater.* **2018**, *14*, 1−7.

DOI: 10.1021/acsami.9b13838
ACS Appl. Mater. Interfaces 2019, 11, 37842−37849